Development of metal-organic framework-derived NiMo-MoO$_{3-x}$ porous nanorod for efficient electrocatalytic hydrogen evolution reactions

Bal Sydulu Singu [a], Ramesh Kumar Chitumalla [b], Debasish Mandal [a], Yongrae Kim [a], Gil Ho Kim [c], Hoon Taek Chung [c], Joonkyung Jang [b,*], Hansung Kim [a,*]

[a] Electrochemical Energy Laboratory, Department of Chemical and Biomolecular Engineering, Yonsei University, Seoul 03722, Republic of Korea
[b] Department of Nanoenergy Engineering, Pusan National University, Busan 46241, Republic of Korea
[c] Hanwha Solutions Chemical Division, H2 Technology R&D Center 76, Gajeong-ro, Yuseong-gu, Daejeon, Republic of Korea

ARTICLE INFO

ABSTRACT

In this study, we developed a noble metal-free HER electrocatalyst NiMo-MoO$_{3-x}$ porous nanorod (NiMo-MoO$_{3-x}$ −PNR) by optimal thermal reduction of NiMoO$_4$ porous nanorod (NiMoO$_4$ −PNR), where the porous structure of NiMoO$_4$ −PNR was enabled by calcining the designed Ni-Mo-metal-organic framework nanorod (Ni-Mo-MOF−NR). As a result of its ideal porous nanorod structure, composition, and improved bifunctional properties, the electrocatalyst demonstrated superior HER performance (a low overpotential of 24.5 mV @ 10.0 mA cm^{-2}) in 1 M KOH, which was comparable with that of state-of-the-art platinum group metals (PGMs) based electrocatalysts. Furthermore, NiMo-MoO$_{3-x}$ −PNR displayed faster Volmer-Tafel mechanism (a small Tafel slope of 32 mV dec^{-1}) for HER process. The superior HER activity of NiMo-MoO$_{3-x}$ −PNR was supported by density functional theory simulations. Moreover, it exhibited a high cyclic stability (unaffected after 100,000 cycles) and robust durability (102 h). Overall, this study demonstrates a simple, scalable, and versatile synthesis of a noble metal-free highly efficient inexpensive electrocatalyst for HER.

1. Introduction

Rising environmental concerns over anthropogenic climate change have highlighted the pressing need to use the renewable and sustainable energy sources capable of serving as eventual replacements for traditional fossil fuels. Hydrogen has a relatively high mass energy density and is anticipated to be an efficient energy carrier [1]. "Green" hydrogen, produced by water electrolysis, is an attractive alternative to "blue" hydrogen, generated through steam reforming of hydrocarbons, for carbon-free pure hydrogen fuel production because it is an environmentally friendly and involved renewable processes [2]. Water electrolysis involves two electrochemical reactions: the cathodic

hydrogen evolution reaction (HER) and the anodic oxygen evolution reaction (OER). In order to optimize the hydrogen production rate, it is important to reduce the overpotential required for each electrochemical reaction. Noble metal-based catalysts, especially platinum, are presently regarded as the most efficient electrocatalysts for HER. However, the long-term feasibility of using such metals is uncertain because of their scarcity and high cost, making them difficult for industrial use [3]. Therefore, low-cost, earth abundant non-platinum group metals (NPGMs)-based catalysts with superior electrocatalytic activity should be investigated as potential substitutes.

Numerous efforts have been made to identify suitable NPGM derivative catalysts, including oxides, sulfides, phosphides, nitrides, and

alloys [4–6]. Among the NPGM derivatives examined, NiMo-alloy was found to be one of the most promising electrocatalysts for HER in alkaline media because of its structural advantages. For example, NiMo has a platinum-like electronic surface state and exhibits a strong synergy between electron-rich Ni and electron-deficient Mo within the alloy [7–9]. NiMo-alloy-based electrocatalysts have been reported in both thin film [9–12] and powder forms [8,13,14]. The electrocatalytic HER performance of thin films (overpotential: 17–178 mV) is superior to that of the powder form (overpotential: 38–340 mV) [8,10,12,15–19]. However, a careful consideration of their relative eases in production scalability and usefulness within alkaline anion exchange membrane (AEM)-based water electrolysis indicates that powder electrocatalyst is the more practical of the two for industrial applications [20,21]. To date, reported NiMo-alloy based powder electrocatalysts have exhibited far poorer performance than commercial Pt/C [8,17,18]. Therefore, for them to be able to replace Pt/C, the successful development of a sufficiently high performing NiMo-alloy-based powder-electrocatalyst is a crucial initial step. To this end, various approaches may be employed to enhance the electrocatalytic performance of NiMo alloys, including modification of chemical composition/electronic structures and synthesizing well-organized porous textures. Several studies have demonstrated that incorporation of metal oxides into metals having optimal hydrogen adsorption energies can accelerate overall HER rates because metal oxides are highly efficient at adsorbing to water molecules and cleaving H—OH bonds [22–25]. Li et al. demonstrated that Ru-O-Mo sites in Ru/MoO_2 catalysts significantly increased its water adsorption capability relative to pure Ru and resultantly exhibited a very small overpotential of only 16 mV at 10 mA cm^{-2} in 1 M KOH, which was much lower than that of the previously reported Ru catalyst [22]. Markovic et al. demonstrated that different metals modified by combining $Ni(OH)_2$ nanoclustures exhibit improved bifunctional properties involved in HER mechanism, i.e. formation of hydrogen intermediates (H*) through electrochemical dissociation of water molecules, and subsequent generation H_2 molecules from H*; consequently, these show significantly improved HER catalytic activity in alkaline solution compared to the respective metals [24]. Therefore, it may be hypothesized that NiMo-alloy-oxide nanohybrid-system may similarly demonstrate an improved catalytic HER activity. Recently, Yang et al. vertically grew NiMo nanosheets on MoO_2 nanoplates, which exhibited much higher HER activity (overpotential: 52 mV @ 10 mA cm^{-2}) than the pure NiMo system [26]. Additionally, porous materials derived from metal-organic frameworks (MOF) have several key advantages over conventional catalysts, including larger surface areas and more versatile morphologies, which are parameters that must be optimized for robust electrocatalytic activity [27].

In this study, we developed a novel NiMo-MoO$_{3-x}$ porous nanorod (NiMo-MoO$_{3-x}$ −PNR) hybrid system to function as efficient HER electrocatalyst via formation of MOF intermediate. To optimize the manufacturing process, we systematically manipulated reaction conditions, such as reduction temperature and gas atmosphere, and quantified the resultant changes in catalyst properties and performance. The morphology, electronic structure, composition, and interactions between alloy and oxide components within the catalyst were investigated using numerous techniques, including microscopic, diffraction, spectral analyses, and BET (Brunauer–Emmett–Teller) isotherms. The electrocatalytic HER performances of the catalyst in 1 M KOH were inspected by several electrochemical assays. The superior HER activity of NiMo-MoO$_{3-x}$ surface was also verified by the density functional theory (DFT) simulations.

2. Experimental

2.1. Reagents

Molybdenum oxide (purity: $\geq$ 99.5%), nickel chloride hexahydrate (purity: 99.9%), imidazole (purity: $\geq$ 99%), and potassium hydroxide (purity: $\geq$ 85%) were procured from Sigma-Aldrich. Pt/C (40 wt%) was purchased from Johnson-Matthey. All chemicals were used as received.

2.2. Synthesis of Ni-Mo metal organic framework nanorod

Molybdenum oxide (1.0 g, 6.91 mmol), nickel chloride hexahydrate (1.65 g, 6.91 mmol), and imidazole (2.70 g, 39.26 mmol) were added in deionized water (DI, 200 ml) within a round-bottom flask and stirred at room temperature for 5 min to obtain a homogeneous dispersion. Subsequently, the mixture was heated and stirred constantly for 24 h at 120 °C under reflux to produce Ni-Mo metal-organic framework nanorod (Ni-Mo-MOF−NR). The product was then isolated using vacuum filtration, washed with DI water, and finally with ethanol. Synthesized pure Ni-Mo-MOF−NR was then dried overnight in an electric oven at 60 °C before further analyses.

2.3. Synthesis of $NiMoO_4$ porous nanorod

$NiMoO_4$ porous nanorod ($NiMoO_4$ −PNR) was produced by calcining Ni-Mo-MOF−NR at 450 °C for 2 h at a heating rate of 2 °C/min under constant air flow. The yield of light yellow $NiMoO_4$ −PNR product was ~70.4 wt%.

2.4. Synthesis of NiMo-MoO$_{3-x}$ porous nanorod

Optimized NiMo-MoO$_{3-x}$ porous nanorod (NiMo-MoO$_{3-x}$ −PNR) was prepared by placing 200 mg of $NiMoO_4$ −PNR in a ceramic boat and heating the vessel at 500 °C in a tube furnace at a heating rate of 5 °C/min for 2 h under the flow of Ar/H$_2$ (70/30% by volume) atmosphere. Black porous NiMo-MoO$_{3-x}$ −PNR (production yield ~77 wt%) was collected after allowing the furnace to cool to room temperature. In addition, the catalysts were prepared at various thermal reduction temperatures ranging from 400 to 800 °C, to investigate the effect of the reduction temperature upon the physical properties and catalytic activities of the respective catalyst preparations. The prepared catalysts were labeled as Ni-Mo–t, where, t referred to the reduction temperature assessed.

2.5. Preparation of NiMo-MoO$_{3-x}$/C nonporous nanorod

The direct thermal reduction of Ni-Mo-MOF−NR produced NiMo-MoO$_{3-x}$/C nonporous nanorod (NiMo-MoO$_{3-x}$/C−NPNR). Here, 200 mg of Ni-Mo-MOF−NR was heated at 500 °C for 2 h in a tube furnace under flowing of Ar/H$_2$ (70/30% by volume) atmosphere. After allowing the tube furnace to naturally cool to room temperature, black NiMo-MoO$_{3-x}$/C−NPNR was collected.

2.6. Structural characterizations

The crystallographic structures of prepared nanostructures were determined using a Rigaku miniFlex (Rigaku, Japan) X-ray diffractometer equipped with Cu Kα radiation, at a scan speed of 2°/min in the 2θ range of 5–90°. The CHN elemental analyses of the samples were performed using a 2400 Series II CHNS/O analyzer (PerkinElmer Co., Ltd.). Thermogravimetric analysis (TGA) was performed in air using a PerkinElmer TGA 8000 thermogravimetric analyzer at a heating rate of 5 °C/min. The morphologies of the prepared materials were examined using field-emission scanning electron microscopy (FE-SEM; JEOL-7800 F). Transmission electron microscopy (TEM), high-resolution transmission electron microscopy (HR-TEM), and energy X-ray spectroscopy (EDS) mapping images were captured using a multipurpose transmission electron microscope (JEM-F200) at an operating voltage of 200 kV. To determine the mass percentages of Ni and Mo in NiMo-MoO$_{3-x}$ −PNR and precursor materials, inductively coupled plasma optical emission spectroscopy (ICP-OES; Thermo Scientific iCAP-6000) measurements were performed after dissolving samples in acid. Samples' surface areas

and pore size distributions were measured using a Quantachrome Instrument Autosorb-iQ 2ST/M. P. The chemical compositions of prepared materials were determined using a Fourier transform infrared (FT-IR) spectrometer (model iS10, Nicolet Nexus, Minnesota). The chemical states of samples were assayed via X-ray photoelectron spectroscopy (XPS, K-alpha, Thermo V.G.) coupled with a monochromatic Al X-ray source (Al Kα line:1486.6 eV, 12 kV, 3 mA).

2.7. Electrochemical measurements

All electrochemical measurements were performed in a standard three-electrode system using an electrochemical workstation (VSP, Biologic). The catalyst ink was prepared by sonicating the catalyst (10 mg) in IPA (0.5 ml) and Nafion (50 μL) for an hour. Then, the catalyst ink was drop-coated onto a rotating ring-disc electrode (RRDE; 5.6 mm in diameter) using a micropipette. The loading amount of prepared catalyst was to 2.94 mg cm^{-2}. The amount of Pt metal content in Pt/C loaded onto RRDE was 0.75 mg cm^{-2}. Analyses were conducted in 1 M KOH (pH = 14) solution using the catalyst-loaded RRDE, Hg/HgO, and graphite rods as working, reference, and counter electrodes, respectively. To activate electrocatalysts, five cyclic voltammetry (CV) cycles were conducted at 1 mV s^{-1} in the potential range of + 0.1 to − 0.5 V vs. reversible hydrogen electrode (RHE). All linear sweep voltammetry (LSV) data were recorded at a rotational speed of 1600 rpm and sweep rate of 5 mV s^{-1}. The Ohmic and charge transfer resistances of electrocatalysts were measured via electrochemical impedance spectroscopy (EIS) in the frequency range of 100 kHz to 100 mHz, at an amplitude of 10 mV. A CV stability test was conducted using RRDE in the potential range of + 0.2 to − 0.25 V vs. RHE for 100,000 cycles, at a sweep rate of 200 mV s^{-1}. All LSV curves were IR-corrected by measuring the Ohmic resistance (R_S) of the electrode in 1 M KOH solution using the EIS method ($E_{IR} = E_M - I \times R_S$; E_{IR} is the IR-corrected potential, E_M is the measured potential, and R_S is the Ohmic resistance). The potential scale vs. Hg/HgO reference electrode was converted to vs. RHE by adding 0.922 V, which was obtained by calibrating the Hg/HgO reference electrode in 1 M KOH by purging H$_2$ gas and using two separate Pt wires as the counter and working electrodes.

2.8. Models and computational details

We performed all the spin-polarized DFT simulations of NiMo and NiMo−MoO$_{3−x}$ employing the Vienna ab initio simulation package (VASP 5.4.1) [28]. We used a periodic supercell of NiMo(101) slab with a total of 162 atoms. The (101) surface has higher electrocatalytic activity than the other low-index NiMo surfaces [29]. A significant vacuum (25 Å) was introduced in the z-direction of the supercell to avoid spurious interactions between repeated slabs. To model the NiMo−MoO$_{3−x}$, we added the oxygen atoms to the Mo atoms of the top layer of the NiMo(101).

In the calculations, the projector-augmented-wave [30] method was used to describe the electronic-ionic core interactions, and the Kohn-Sham orbitals were expanded using a plane-wave basis set with a kinetic energy cutoff of 450 eV. To model the exchange–correlation, we used the generalized gradient approximation (GGA) with the Perdew–Burke–Ernzerhof (PBE) functional [31]. As in our previous study [32], the geometries were fully relaxed until the maximal energy difference is less than 10^{-5} eV and the Hellmann-Feynman force on every atom is less than 0.02 eV Å^{-1}. During the geometry optimization, only the top layers and the adsorbates (H$_2$O and H*) were fully relaxed, while all the atoms in the bottom layer of the slab were held fixed. For all simulations, we use the Monkhorst-Pack scheme with $1 \times 1 \times 1$ k-points to sample the Brillouin zone. We have calculated the energy barriers of the transition state of the H$_2$O dissociation step by employing the nudged elastic band (NEB) method as implemented in VASP. The free energy changes of H$_2$O and H* adsorption on NiMo and NiMo−MoO$_3$ surfaces have been obtained by employing widely used methods [12,

33].

3. Results and discussion

3.1. Synthesis and characterization

The steps of NiMo-MoO$_{3−x}$ −PNR synthesis and corresponding reaction mechanisms are illustrated in Fig. 1. It was synthesized in three steps. In the first step, a uniform nonporous Ni-Mo metal-organic framework nanorod (Ni-Mo-MOF−NR) was synthesized by refluxing MoO$_3$, NiCl$_2$, and imidazole as monomers. Notably, the reaction between MoO$_3$ and imidazole only occurred in the presence of NiCl$_2$. During the reaction, an imidazole molecule covalently bonded MoO$_3$ by transferring the lone pair electrons of its two N atoms to Mo. The resultant two Mo– O$^-$ bonds were neutralized via ionic bonding with Ni^{2+}. So, the atomic ratio of Ni to Mo in Ni-Mo-MOF−NR always remained at approximately 1:1, even when the molar ratios of NiCl$_2$ and MoO$_3$ precursors were varied (Table S1). This reaction mechanism led to one-dimensional growth of the MOF, resulting in nanorod morphology. In the second step, during the annealing of Ni-Mo-MOF−NR in an air atmosphere, thermal decomposition of the imidazole backbone was accompanied which facilitated the formation of NiMoO$_4$ porous nanorod (NiMoO$_4$ −PNR). The thermal decomposition of the imidazole backbone was also confirmed by performing thermogravimetric analysis (TGA) of Ni-Mo-MOF−NR (Fig. S1). The mass loss in the second step (29.6%) was found to be identical to the mass loss during TGA (29.5%) of Ni-Mo-MOF−NR. Finally, in the third step, a thermal reduction of NiMoO$_4$ −PNR at 500 °C, under an Ar/H$_2$ atmosphere, produced NiMo-MoO$_{3−x}$ porous nanorod (NiMo-MoO$_{3−x}$ −PNR).

The chemical structures of prepared Ni-Mo-MOF−NR, NiMoO$_4$ −PNR, and NiMo-MoO$_{3−x}$ −PNR were investigated using FT-IR spectroscopy (Fig. 2a). As shown in Fig. 2a, the FT-IR spectrum of Ni-Mo-MOF−NR exhibited characteristic stretching bands at 3430 cm^{-1} (O–H of adsorbed H$_2$O), 2800–3000 cm^{-1} (C–H), 1630 cm^{-1} (C=C), and 1200–1400 cm^{-1} (C–N/C=N) for the imidazole backbone [34], where FTIR bands at 1260, 933, 874, and 651 cm^{-1} were attributed to Mo–N, Mo=O, Mo–O, and Ni–O bonds, respectively [35]. The characteristic FTIR bands of NiMoO$_4$ −PNR at 807 and 879 cm^{-1} for the Mo–O–Mo bond, 965 cm^{-1} for the Mo=O bond, and 633 cm^{-1} for the Ni–O bond confirmed the successful formation of NiMoO$_4$ [36,37] from Ni-Mo-MOF−NR precursor via removal of the imidazole backbone during calcination in air. In the case of NiMo-MoO$_{3−x}$ −PNR, the transmittance of the FTIR spectrum increased significantly (>0.95) due to alloy formation. The presence of some less intense characteristic FTIR peaks of molybdenum oxide in the region 1000–500 cm^{-1} indicated existence of some amount of molybdenum oxide in NiMo-MoO$_{3−x}$ −PNR. The FTIR band at 927 cm^{-1} was assigned to the Mo=O stretching vibration, while the FTIR bands at 852 and 734 cm^{-1} were assigned to the Mo-O-Mo stretching mode of MoO$_3$ and MoO$_2$, respectively; And the FTIR band at 578 cm^{-1} was assigned to the triply coordinated oxygen (Mo$_3$–O) stretching mode of MoO$_3$ [38,39].

The specific surface areas and pore structures of synthesized Ni-Mo-MOF−NR, NiMoO$_4$ −PNR, and NiMo-MoO$_{3−x}$ −PNR samples were investigated using Brunauer–Emmett–Teller (BET) surface analysis (Fig. 2b). Their surface areas were 20.0, 74.5, and 61.6 m^2 g^{-1}, respectively. Furthermore, average pore diameters and pore volumes of Ni-Mo-MOF−NR, NiMoO$_4$ −PNR, and NiMo-MoO$_{3−x}$ −PNR were determined to be 21.3, 10.0 and 7.4 nm and 0.05, 0.32, and 0.21 cm^3 g^{-1}, respectively, indicating that Ni-Mo-MOF−NR had no significant porosity. Due to the decomposition of its imidazole backbone during its calcination, mesopores were generated in NiMoO$_4$ −PNR and this porous structure was retained even during thermal reduction of NiMoO$_4$ −PNR into NiMo-MoO$_{3−x}$ −PNR. In contrast, direct thermal reduction of Ni-Mo-MOF−NR to NiMo-MoO$_{3−x}$/C− NPNR produced a dense nonporous substance with a nanorod morphology. It exhibited a very poor specific surface area of only 6.8 m^2 g^{-1} and a negligible pore volume of
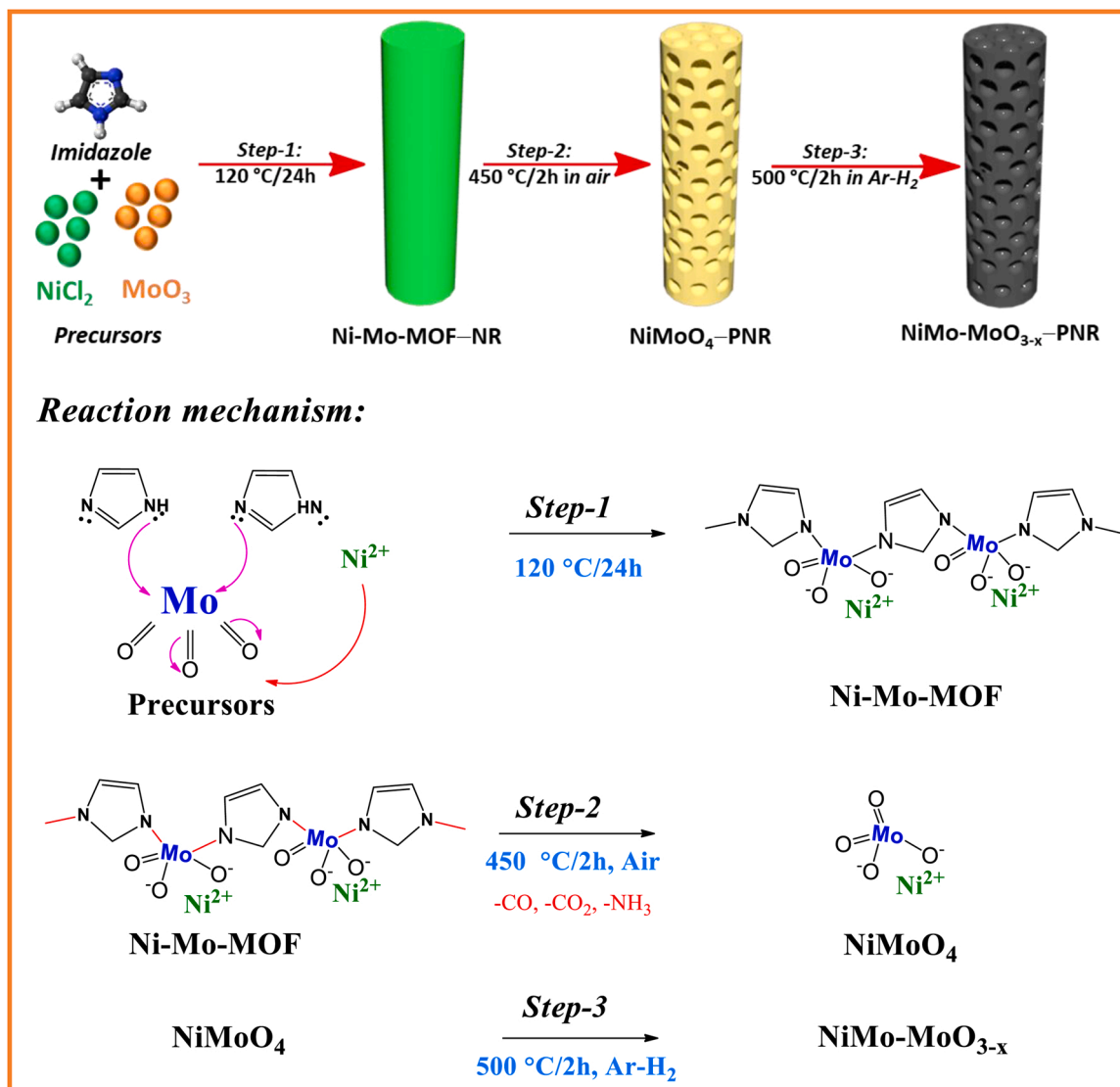
Fig. 1. Graphical illustration of the synthesis of Ni-Mo-MOF−NR, NiMoO$_4$ −PNR and NiMo-MoO$_{3-x}$ −PNR, and the corresponding reaction mechanism of each step.
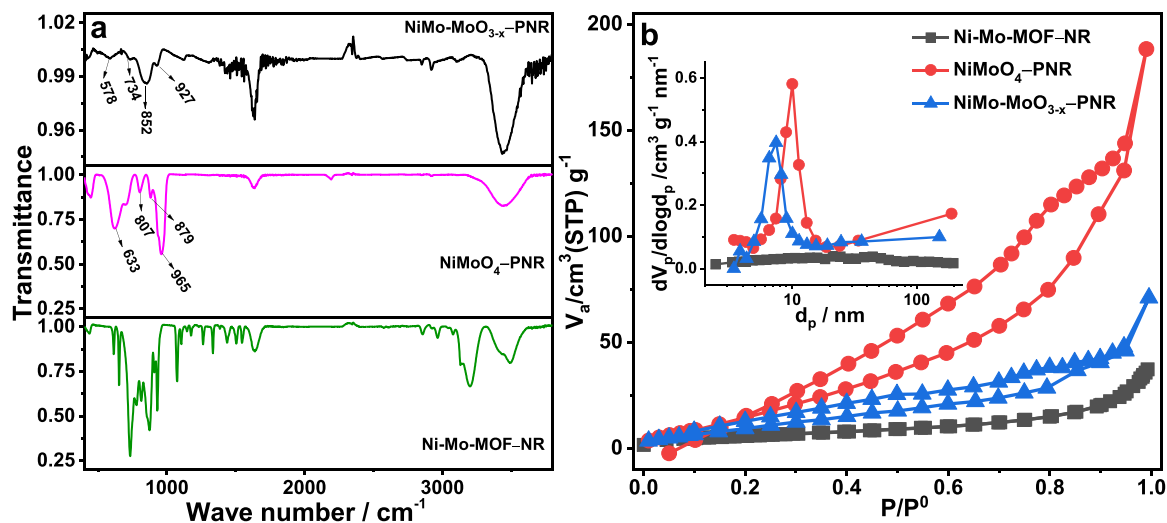

Fig. 2. a) FT-IR and b) BET analysis of Ni-Mo-MOF−NR, NiMoO$_4$ −PNR, and NiMo-MoO$_{3-x}$ −PNR. In b), inset of N$_2$-adsorption/desorption isotherms' plot, corresponding pore size distribution curves are shown.

0.081 cm^3 g^{-1} (Fig. S2). The larger surface area and high pore volume of NiMo-MoO$_{3-x}$ −PNR catalyst may result in better contact with the electrolyte, leading to more rapid ion transport and enhanced active site generation, which could increase catalytic activity [40–42].

The morphologies of prepared materials were investigated via field-emission scanning electron microscopy (FE-SEM) and transmission electron microscopy (TEM). The FE-SEM image presented in Fig. 3a indicates that the MoO$_3$ precursors we received from the vendor had a microparticle structure. Synthesized Ni-Mo-MOF−NRs exhibited a nanorod morphology with a smooth surface having a diameter of 100–400 nm, and a length of several micrometers (Fig. 3b). The NiMoO$_4$ −PNR obtained via calcination of Ni-Mo-MOF−NR retained its nanorod morphology and developed a porous structure and rough surface (Fig. 3c), as the presence of organic ligands was carefully eliminated during the calcination process. As shown in Fig. 3d and e, the porous-nanorod morphology of NiMoO$_4$ −PNR was well preserved in NiMo-MoO$_{3-x}$ −PNR after undergoing the thermal reduction process at 500 °C, and was consistent with BET-isothermal and pore distribution analyses. In contrast, NiMo-MoO$_{3-x}$/C−NPNR exhibited a nonporous, compact nanorod morphology, as shown in Fig. S3 (Table S2). Further, TEM (Fig. S4) demonstrated that the porous nanorod morphology of the catalyst was preserved when it was prepared by thermal reduction of NiMoO$_4$ −PNR at ≤ 600 °C. At higher temperatures (700/800 °C) however, its normally porous nanorod morphology was transformed
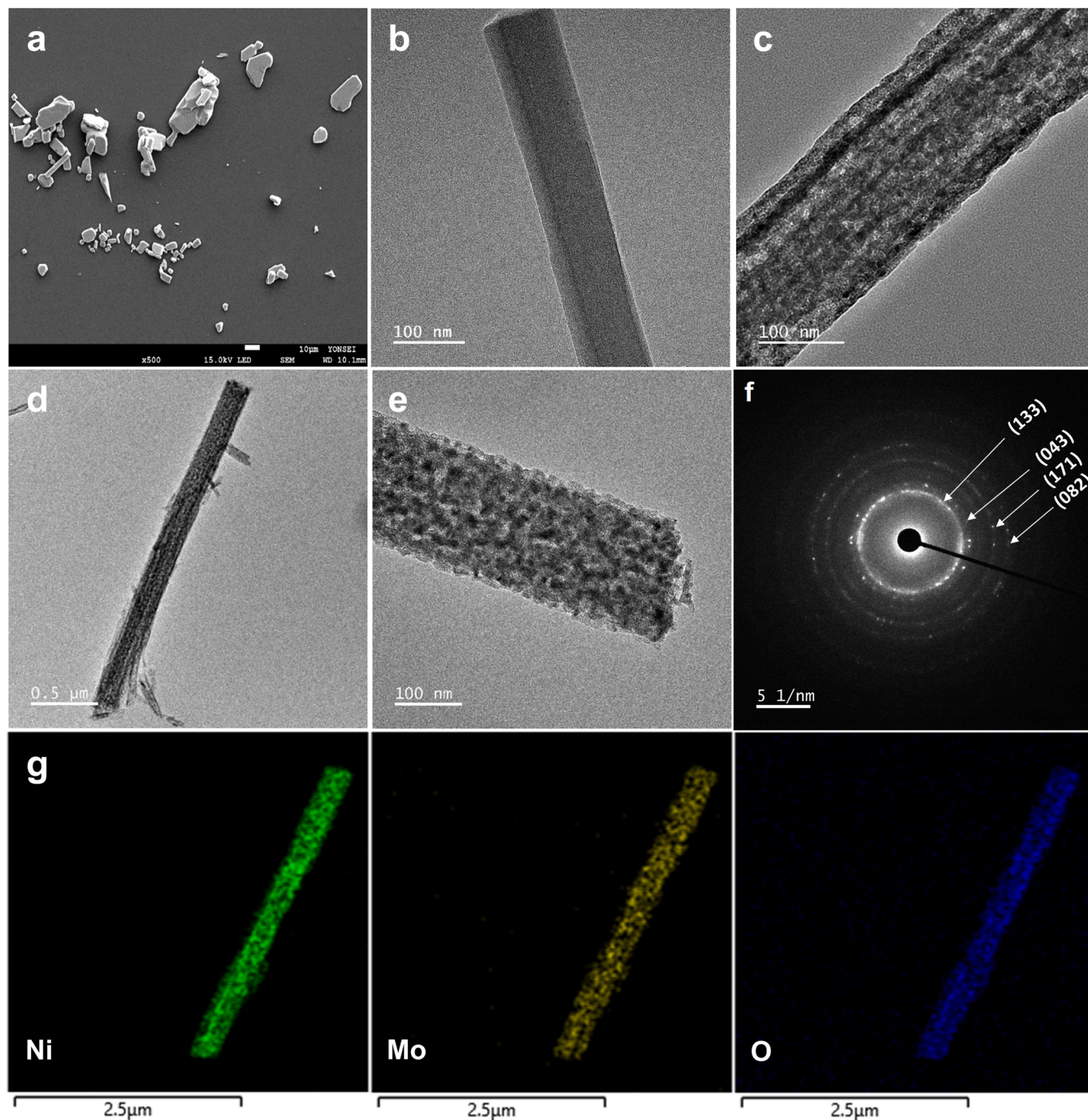

Fig. 3. a) FESEM image of MoO$_3$, TEM images of b) Ni-Mo-MOF−NR, c) NiMoO$_4$ −PNR, and d, e) NiMo-MoO$_{3-x}$ −PNR. f) SAED pattern and g) EDAX mapping analysis of NiMo-MoO$_{3-x}$ −PNR.

into a nonporous, squeezed state. The TEM results were supported by BET analysis, which revealed that the porous nanorods structures were thermally stable up to 600 °C, after which their surface area and pore volume collapsed, indicating their transition from porous to nonporous structures (Fig. S5 and Table S3). The selected area electron diffraction (SAED) pattern of NiMo-MoO_{3-x} −PNR (Fig. 3f) shows four continuous diffraction rings identified as NiMo alloy planes ((133), (043), (171), and (082)), indicating that NiMo-MoO_{3-x} −PNR was polycrystalline. Elemental mapping of NiMo-MoO_{3-x} −PNR (Fig. 3g) indicated that Ni, Mo, and O were uniformly dispersed. The presence of O was attributed to the molybdenum oxides.

The crystal structures of prepared materials were next characterized via XRD pattern analyses. The XRD pattern of Ni-Mo-MOF−NR (Fig. S6) revealed a few diffraction peaks identical to those of Ni-MOF, Mo-MOF, and $NiMoO_4$, which implies that the formation of Ni-Mo-MOF−NR was successful [43,44]. The XRD pattern of $NiMoO_4$ −PNR (Fig. 4 and S6) matched the standard diffractogram of monoclinic $NiMoO_4$ (JCPDS no:00–045–0142). As shown in Fig. 4, the diffractogram of NiMo-MoO_{3-x} −PNR prepared at a reduction temperature of 500 °C mainly exhibited XRD patterns characteristic of an orthorhombic NiMo-alloy state (JCPDS no:00–048–1745) [8,45], suggesting a successful reduction of $NiMoO_4$ to NiMo-alloy. Furthermore, we investigated the reduction temperature-dependent crystal phases of the catalysts via XRD analyses (Fig. 4). The reduction temperature employed during synthesis exerted a significant effect on the crystal phase of prepared catalysts. The XRD pattern of catalyst synthesized at 400 °C almost matched that of catalyst synthesized at 500 °C, where the XRD peaks of NiMo phase were intense and perfectly located when catalyst was synthesized at 500 °C. However, when catalyst was prepared at $\geq$ 600 °C, and even more so at $\geq$ 700 °C, the XRD pattern observed had Mo-metal (JCPDS no:00–001–1207) and Ni_3Mo-alloy (JCPDS no:03–065–5305) components. This indicated that at higher temperatures, catalyst split into Ni_3Mo-alloy and Mo-metal forms. As shown within Fig. S7, the XRD pattern of NiMo-MoO_{3-x}/C−NPNR nearly matched with that of NiMo-MoO_{3-x} −PNR, indicating highly similar crystal structures.

The composition and electronic states of the prepared materials were next inspected using XPS (Figs. S8, 5 and 6). As observed in the survey spectra in Fig. S8, when Ni-Mo-MOF−NR was calcined to produce $NiMoO_4$ −PNR, a significant decrease in the intensity of the C1s XPS peak was observed. This suggested an elimination of the imidazole backbone during the calcination process. The presence of small C1s peaks in $NiMoO_4$ −PNR and NiMo-MoO_{3-x} −PNR samples may be due to residual carbon left over from calcination or from the environment. These small peaks are common to all XPS spectra [46,47]. In the case of
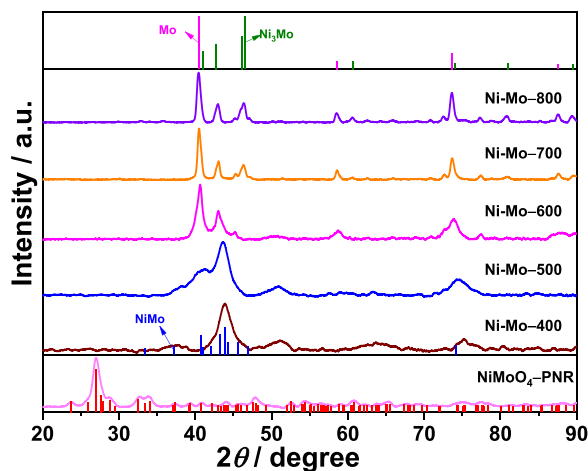
nitrogen, it is difficult to confirm the existence of nitrogen in the XPS spectra because the N1s and $Mo3p_{3/2}$ peaks overlap each other at almost the same position ($\approx$ 400 eV). However, the presence of N can be inferred by calculating the peak-area ratio at $\approx$ 400 eV (sum of $Mo3p_{3/2}$ and N1s peaks) and $\approx$ 415 eV ($Mo3p_{1/2}$ peaks). The area ratio of $Mo3p_{3/2}$ and $Mo3p_{1/2}$ peaks should be 2:1 according to the degeneracy numbers of $3p_{3/2}$ and $3p_{1/2}$ levels. As shown in Table S4, this ratio was much higher (2.71:1) for the NiMo-MOF−NR, indicating the presence of a significant amount of nitrogen. On the other hand, the ratio was close to 2:1 for $NiMoO_4$ −PNR and NiMo-MoO_{3-x} −PNR, indicating that N was removed during the calcination of NiMo-MOF−NR in air. It was also confirmed by CHN elemental analysis (Table S5). When $NiMoO_4$ −PNR was thermally reduced to NiMo-MoO_{3-x} −PNR at 500 °C, its O1s peak intensity decreased significantly, signifying a reduction of $NiMoO_4$ to an alloyed state with the presence of some oxide content.

The deconvoluted HR-XPS spectra of Ni-Mo-MOF−NR and $NiMoO_4$ −PNR shown in Fig. 5 had similar Ni 2p and Mo 3d peaks for Ni^{2+} and Mo^{6+} states, respectively. The deconvoluted Ni-2p HR-XPS spectrum of NiMo-MoO_{3-x} −PNR showed two distinct peaks at 853.04 and 870.24 eV, which correspond to Ni^0-$2p_{3/2}$ and Ni^0-$2p_{1/2}$, respectively; both peaks were accompanied by two Ni^0 satellite peaks. These results demonstrate that Ni^{2+} state in $NiMoO_4$ was reduced to Ni^0 state in NiMo-MoO_{3-x} −PNR during thermal reduction. Furthermore, the higher binding energy of Ni^0 state (853.04 eV) in NiMo-MoO_{3-x} −PNR compared to that of the pure Ni-metal (852.6 eV) indicated the existence of NiMo alloy state, where electron transferred from electron-rich Ni-center to electron-deficient Mo-center. The deconvoluted Mo-3d HR-XPS spectrum of NiMo-MoO_{3-x} −PNR displayed six distinct peaks for Mo^0, Mo^{4+} and Mo^{6+} valance states. These findings specified the presence of oxide states with NiMo alloy state. The presence of molybdenum oxide was also confirmed by FTIR analysis (Fig. 2a). The ICP-OES analysis (Table 1) revealed that the atomic ratio of Ni and Mo in the NiMo-MoO_{3-x} −PNR was 1:1. Therefore, the chemical formula of the NiMo-MoO_{3-x} −PNR catalyst can be expressed as the $NiMo_{1-y}$-$yMoO_{3-x}$ ($0 < y < <1$; $0 < x < 1$).

Interestingly, the Mo^0-state in NiMo-MoO_{3-x} −PNR electrocatalyst exhibited a large positive binding energy (BE) shift (BE of 228.55 eV for Mo^0-$3d_{5/2}$) compared to pure Mo-metal (BE of 227.94 eV for Mo^0-$3d_{5/2}$) [48], though, the general tendency in NiMo-alloy system is to transfer electrons from electron-rich Ni to electron-deficient Mo. In addition, the Mo^{+6} state in NiMo-MoO_{3-x} −PNR electrocatalyst exhibited a substantially lower BE in the catalyst (BE of 231.34 eV for Mo^{+6}-$3d_{5/2}$) compared to pure MoO_3 (BE of 233.1 eV for Mo^{+6}-$3d_{5/2}$) as well as Ni-Mo-MOF−NR and $NiMoO_4$ −PNR precursors (BE of $\approx$232.7 eV for Mo^{+6}-$3d_{5/2}$). The similar effect was observed in the Mo^{+4} state of the NiMo-MoO_{3-x} −PNR electrocatalyst, where Mo^{4+} has a lower binding energy (BE of 229.6 eV for Mo^{+4}-$3d5/2$) than in pure MoO_2 (BE of 229.9 eV for Mo^{+4}-$3d5/2$). These findings imply that electron transport occurs from Ni^0 to Mo^0 and Mo^0 to molybdenum oxide, establishing the formation of a NiMo-MoO_{3-x} nanohybrid structure with significant synergy between its alloy and oxide components. To further understand the controlling factor of the synergistic effect, Ni-MoO_3 material was prepared (Fig. S9) and confirmed by XPS study (Fig. S10). The shift in the BE of Mo^{6+} in Ni-MoO_3 (231.93 eV for Mo^{+6}-$3d_{5/2}$) was 1.17 eV, whereas the shift in the BE of Mo^{6+} in NiMo-MoO_{3-x} (231.36 eV for Mo^{+6}-$3d_{5/2}$) was 1.74 eV relative to pure MoO_3 (233.1 eV for Mo^{+6}-$3d_{5/2}$) (Fig. S10). The large shift in BE indicated that NiMo-MoO_{3-x} exhibited a higher synergistic effect than Ni-MoO_3 because NiMo-alloy particles are stronger electron donors than Ni metal particles. These results imply Mo^0 acts as a bridge between Ni^0 and oxide particle in NiMo-MoO_{3-x} and plays an important role in the synergistic effect as an electron acceptor and donor and.

In addition, XPS was used to investigate the effect of annealing temperature on the chemical composition, chemical states, and synergistic properties of prepared catalysts (Fig. 6). The catalyst prepared at 400 °C showed that the oxide peaks (Ni^{2+}, Mo^{4+}, and Mo^{6+}) strongly
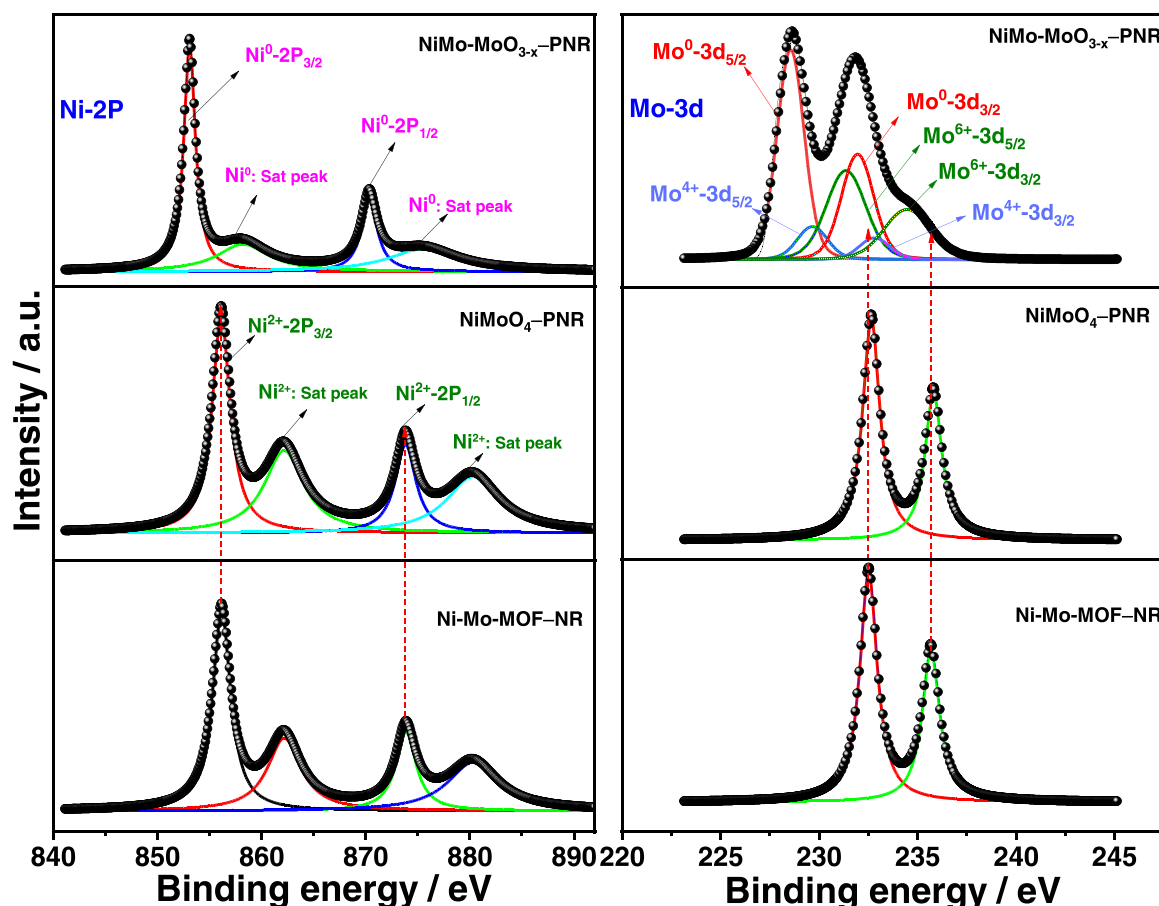

Fig. 4. XRD of $NiMoO_4$ −PNR and catalysts prepared at different reduction temperatures (400–800 °C).
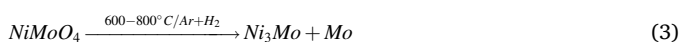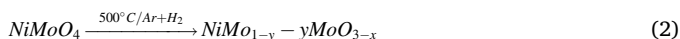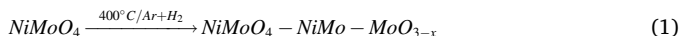
Fig. 5. XPS analysis of Ni-Mo-MOF−NR, NiMoO$_4$ −PNR, and NiMo-MoO$_{3−x}$ −PNR: Deconvoluted Ni-2p and Mo-3d core spectra.

predominated over the alloy peaks (Ni^0 and Mo^0), confirming the incomplete reduction of NiMoO$_4$ and its potential chemical composition of NiMoO$_4$-NiMo-MoO$_{3−x}$. Whereas, the catalysts prepared at ≥ 600 °C shows only alloy peaks (Ni^0 and Mo^0), evidencing maximum reduction of the NiMoO$_4$. Interestingly, they experienced a lower binding energy shift for both the Ni^0 and Mo^0 states than for catalyst prepared at 500 °C. This occurred because of the absence of molybdenum oxide content and splitting of Mo metal from the alloy (cf. by XRD analysis) and ultimately resulted in less synergy between Ni and Mo in the catalyst. Therefore, catalyst prepared at 500 °C exhibited a metal alloy-oxide nanohybrid structure with the highest interactions occurring amongst Ni, Mo, and MoO$_3$. Thus, combining the above experimental results, the chemical formulas of the catalysts synthesized at various reduction temperatures were as follows:

$$NiMoO_4 \xrightarrow{400°C/Ar+H_2} NiMoO_4 - NiMo - MoO_{3-x} \quad (1)$$

$$NiMoO_4 \xrightarrow{500°C/Ar+H_2} NiMo_{1-y} - yMoO_{3-x} \quad (2)$$

$$NiMoO_4 \xrightarrow{600-800°C/Ar+H_2} Ni_3Mo + Mo \quad (3)$$

3.2. Electrocatalytic HER performance of NiMo-MoO$_{3−x}$ −PNR catalyst

The electrocatalytic HER activities of synthesized catalysts and their precursors were evaluated in 1.0 M KOH using linear sweep voltammetry (LSV), at a scan rate of 5 mV s^{-1}, and compared with those of commercial Pt/C. As shown in Fig. 7a, the NiMo-MoO$_{3−x}$ −PNR electrocatalyst prepared at 500 °C exhibited comparable HER performance to commercial Pt/C, while its precursors had very negligible performances. HER activity of NiMo-MoO$_{3−x}$ −PNR was significantly improved relative to NiMo-MoO$_{3−x}$/C−NPNR because of the greater porosity of NiMo-MoO$_{3−x}$ −PNR. Fig. 7b shows that Ni-Mo− 500 (NiMo-MoO$_{3−x}$ −PNR) exhibits the highest HER activity among catalysts prepared at different reduction temperatures. The electrocatalytic HER activities of the catalysts prepared under different conditions have been ordered by their activity levels and are as follows: Ni-Mo− 500 (NiMo-MoO$_{3−x}$ −PNR) > Ni-Mo− 600 > Ni-Mo− 400 > NiMo-MoO$_{3−x}$/C−NPNR > Ni-Mo− 700 > Ni-Mo− 800. The LSV plot derived overpotentials to produce 10 mA cm^{-2} current density for Pt/C and all prepared catalysts including their precursors are summarized in Fig. 7c. Among all synthesized catalysts Ni-Mo− 500 exhibited the lowest overpotential of 24.5 mV, which was comparable to the commercial Pt/C (20.1 mV). To investigate HER kinetics and reaction mechanisms, Tafel plots were derived from the polarization curves, and presented in Figs. 7d and S11. As expected, Ni-Mo− 500 exhibited a very low Tafel slope of 32.0 mV dec^{-1}, which was lowest among all prepared catalysts and was also comparable to commercial Pt/C (28.5 mV dec^{-1}) and reported Pt/C catalysts (21–30.9 mV dec^{-1} in 1 M KOH, and 14–33 mV dec^{-1} in 0.5 M H$_2$SO$_4$) [16,49–52]. The low Tafel slope of Ni-Mo− 500 revealed a more favorable and faster HER kinetics. Typically, in a basic solution, electrocatalytic HER process follows two mechanisms: either Volmer-Tafel [(4) + (5)] or Volmer-Heyrovsky [(4) + (6)], as presented below [53] Volmer reaction

$$H_2O + e^- \rightarrow H^* + OH^- \quad (4)$$

Tafel reaction

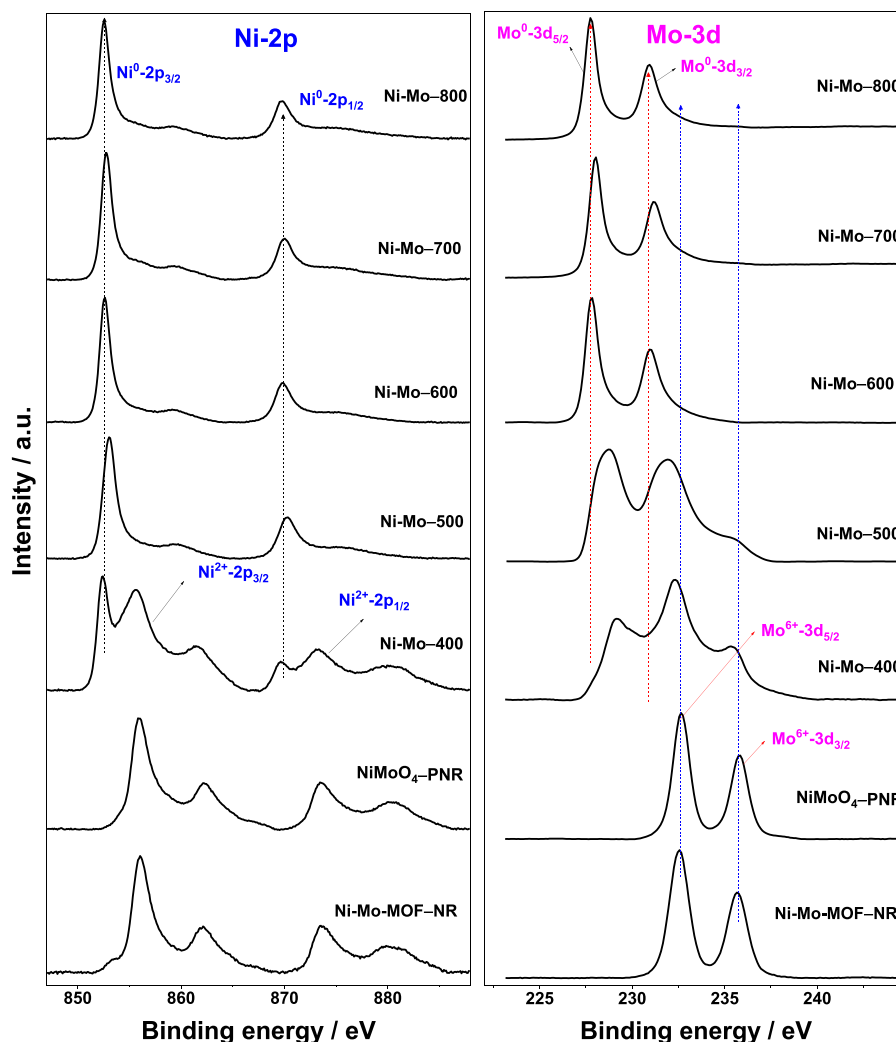$$2H^* \rightarrow H_2 \quad (5)$$

Heyrovsky reaction

Fig. 6. XPS analysis of catalysts prepared at different reduction annealing temperatures (400–800 °C): Ni-2p and Mo-3d core spectra.

Table 1
ICP-OES analysis of Ni-Mo-MOF−NR, NiMoO$_4$ −PNR and NiMo-MoO$_{3-x}$ −PNR.

Element	Ni-Mo-MOF−NR (at%)	NiMoO$_4$ −PNR (at%)	NiMo-MoO$_{3-x}$ −PNR (at%)
Ni	7.56	15.75	31.43
Mo	7.42	15.62	31.88

$$H^* + H_2O + e^- \rightarrow H_2 + OH^- \qquad (6)$$

According to the classical theory on catalytic mechanisms, the low Tafel slope close to 30 mV dec^{-1} indicates that the HER process for Ni-Mo− 500 catalyst followed the faster Volmer-Tafel mechanism, and the corresponding rate determining step was chemical hydrogen desorption (Tafel step)[54]. Such an outstanding electrocatalytic HER performance of NiMo-MoO$_{3-x}$ −PNR (overpotential of 24.5 mV, and Tafel slope of 32.0 mV dec^{-1}) outperformed those of state-of-the-art NPGMs-based powder electrocatalysts including Ni-Mo-alloy-based catalysts, and moreover, it exhibited a parallel performance with commercial Pt/C (20.1 mV, 28.5 mV dec^{-1}) and recently reported PGMs-based electro-catalysts including Ru/D-NPC (23 mV, 38 mV dec^{-1}) [55], Pt@CoS (28 mV, 31 mV dec^{-1}) [56], and Ru/MoO$_{2-x}$ (29 mV, 22 mV dec^{-1}) [57] (Table S6). Such a remarkable HER activity of NiMo-MoO$_{3-x}$ −PNR can be attributed to the superior bifunctional properties of its ideal metal alloy-oxide system and its porous nanorod morphology.

To gain deeper insights into the HER activity of NiMo−MoO$_{3-x}$ hybrid system, we conducted DFT simulations. As the adsorption of the water molecule and subsequent dissociation of the O-H bond is considered a kinetic limiting step in the HER process [58], we evaluated the free energy changes associated with H$_2$O and H* adsorption. In addition, calculated energy barriers of the transition state of O-H bond dissociation facilitated the assessment of the HER activity of NiMo and NiMo−MoO$_{3-x}$. First, the pre-optimized water molecule was adsorbed onto the NiMo and NiMo−MoO$_{3-x}$ surfaces, and the most stable geometries of the adsorbed systems are shown in Fig. 8a. On the NiMo surface, the H$_2$O was adsorbed at different adsorption sites, viz, at the Ni center, Mo center, and above the Ni−Mo bond to identify the effective adsorption site. We have calculated the adsorption free energy of H$_2$O (ΔG_{H_2O}) on NiMo at three sites (vide supra). As shown in Fig. 8b, on the NiMo surface, the Mo center exhibited a more negative ΔG_{H_2O} value (−0.88 eV) than that of the Ni center (−0.29 eV) and Ni−Mo bond center (−0.80 eV). The more negative ΔG_{H_2O} value at the Mo center indicated the preferred H$_2$O molecule adsorption at this center, and so, our further study on NiMo−MoO$_{3-x}$ was limited to the Mo center. The more negative ΔG_{H_2O} value (−0.99 eV) exhibited by the Mo center of NiMo−MoO$_{3-x}$ surface (Fig. 8b) compared to that of the NiMo (−0.88 eV) revealed the strong H$_2$O adsorption on the NiMo−MoO$_{3-x}$, which is favorable to the O−H bond dissociation. The energy barriers of the O−H bond braking step obtained from the NEB simulations are 1.09 and 0.79 eV, for NiMo and NiMo−MoO$_3$, respectively (Fig. 8c). The lower energy barrier on the NiMo−MoO$_{3-x}$ surface indicates that the surface is more effective and alleviates fast O−H bond dissociation
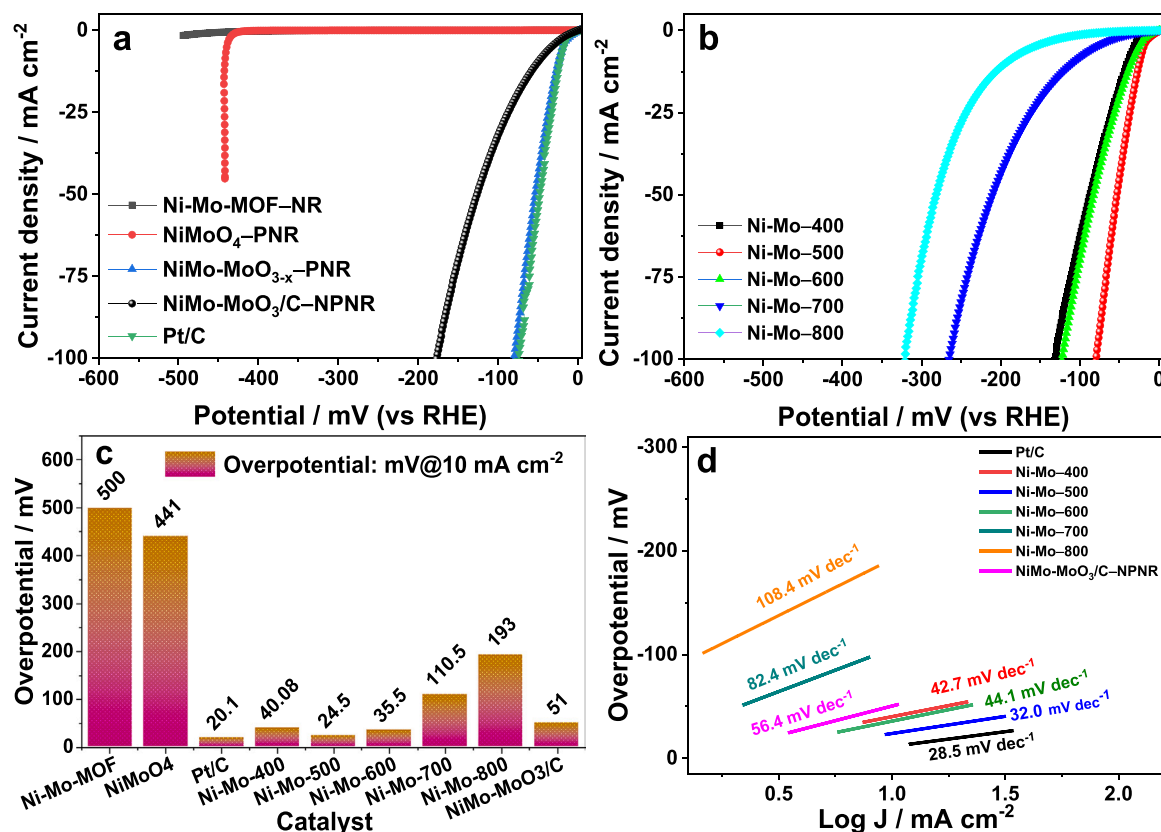
Fig. 7. LSV polarization curves of a) NiMo-MoO$_{3-x}$ −PNR, its precursors, NiMo-MoO$_3$/C−NPNR and Pt/C, b) Ni-Mo−x prepared at different reduction temperatures, c) overpotentials of various catalysts, d) Tafel Plots of different catalysts.

compared to the NiMo surface. After the O−H bond dissociation, the OH remains at the Mo center, whereas, the H is shifted to the Ni center, and subsequent H$_2$ evolution occurs. The Ni center is preferred for H$_2$ evolution over the Mo center due to the lower hydrogen chemisorption energy at the Ni center [12] Further, adsorption free energy of H* (ΔG_{H^*}) plays a prominent role in the assessment of the HER performance of the electrocatalyst. In general, an efficient HER electrocatalyst has a moderate ΔG_{H^*} value near to zero ($\Delta G_{H^*} \approx 0$ eV) and significantly high positive/negative ΔG_{H^*} values lead to poor HER performance [59,60]. As shown in Fig. 8d, the calculated ΔG_{H^*} value of NiMo (0.53 eV) is significantly higher than that of NiMo−MoO$_{3-x}$ (0.16 eV). The lower ΔG_{H^*} value of NiMo−MoO$_{3-x}$ is favorable to the H* adsorption and thereby facilitates the HER performance. The overall DFT study conclude that NiMo−MoO$_{3-x}$ hybrid system is more favorable for HER kinetics, and these theoretical findings are consistent with our experimental HER activity of NiMo−MoO$_{3-x}$ −PNR. Among all catalysts, only the NiMo-MoO$_{3-x}$ −PNR prepared at 500 °C exhibited an optimal metal alloy-oxide nanohybrid system (NiMo$_{1-y}$-yMoO$_{3-x}$) with strong synergy among its Ni, Mo, and MoO$_3$ contents (c.f. by XPS analysis). Therefore, NiMo-MoO$_{3-x}$ −PNR prepared at 500 °C demonstrated the highest HER activity among the all synthesized catalyst. Moreover, the porous 1D nanorod morphology of NiMo-MoO$_{3-x}$ −PNR with large specific surface area assisted in rapid charge transport during electrolysis and maintained availability of electrolyte in good contact with the electrode. As a result, the overall HER performance of NiMo-MoO$_{3-x}$ −PNR improved. In contrast, despite having a similar chemical composition, the nonporous morphology of NiMo-MoO$_{3-x}$/C−NPNR exhibited much lower HER activity than NiMo-MoO$_{3-x}$ −PNR.

The insights into the superior HER performance of NiMo-MoO$_{3-x}$ −PNR were investigated by the analysis of electrochemical impedance spectroscopy (EIS) illustrated in Fig. S12. The charge transfer resistance (R$_{ct}$) relates to the kinetics of electrocatalysis. Namely, a lower R$_{ct}$ value

corresponds to a faster charge-transfer rate [8,61]. NiMo-MoO$_{3-x}$ −PNR exhibited the lowest R$_{ct}$ value among its precursors (Fig. S12a) as well as other synthesized catalysts, including NiMo-MoO$_{3-x}$/C−NPNR (Fig. S12b and c), and was even comparable to Pt/C (Fig. S12c). The low R$_{ct}$ value of NiMo-MoO$_{3-x}$ −PNR was attributed to its porous nanorod structure with its large surface area and improved hydrophilicity with good conductivity enabled by its alloy-oxide hybrid-structure, which in turn increased its HER catalytic activity. To interpret the origin of NiMo-MoO$_{3-x}$ −PNR's high catalytic activity, double-layer capacitance (C$_{dl}$) was measured from the cyclic voltammetry plot (Fig. S13) to obtain the electrochemical surface area (ECSA, ECSA∝C$_{dl}$). The C$_{dl}$ of NiMo-MoO$_{3-x}$ −PNR (259.2 mF cm^{-2}) was significantly larger than that of Ni-Mo− 400 (187.4 mF cm^{-2}) and Ni-Mo− 600 (112.2 mF cm^{-2}). As a result, NiMo-MoO$_{3-x}$ −PNR exhibited superior HER activity [62].

3.3. Cycle life and durability test of NiMo-MoO$_{3-x}$ −PNR

The stability of an electrocatalyst during electrolysis is an important concern for practical applications. The catalytic stability of NiMo-MoO$_{3-x}$ −PNR was investigated via CV and chronopotentiometry (CP) studies using an RRDE, and the results are shown in Fig. 9 and compared with other systems in Table S6. The CV cycles were carried out for 100,000 cycles. The polarization curves of NiMo-MoO$_{3-x}$ −PNR before and after the 100,000 cycles (Fig. 9a) indicated its almost unaffected cyclic stability. As evident in Fig. 9b, NiMo-MoO$_{3-x}$ −PNR maintained an almost invariant overpotential at a current density of 10 mA cm^{-2} during CV cycling. The durability of NiMo-MoO$_{3-x}$ −PNR catalyst was examined by conducting successive CP (V-t) tests at 10 mA cm^{-2} for 1 h, 50 mA cm^{-2} for 100 h, and 10 mA cm^{-2} for 1 h, as summarized in Fig. 9c. The overpotential remained almost unaffected during the CP test. Periodic fluctuations in the V-t profile were observed because of the accumulation and bursting of H$_2$ bubbles at the catalyst surface. The LSV
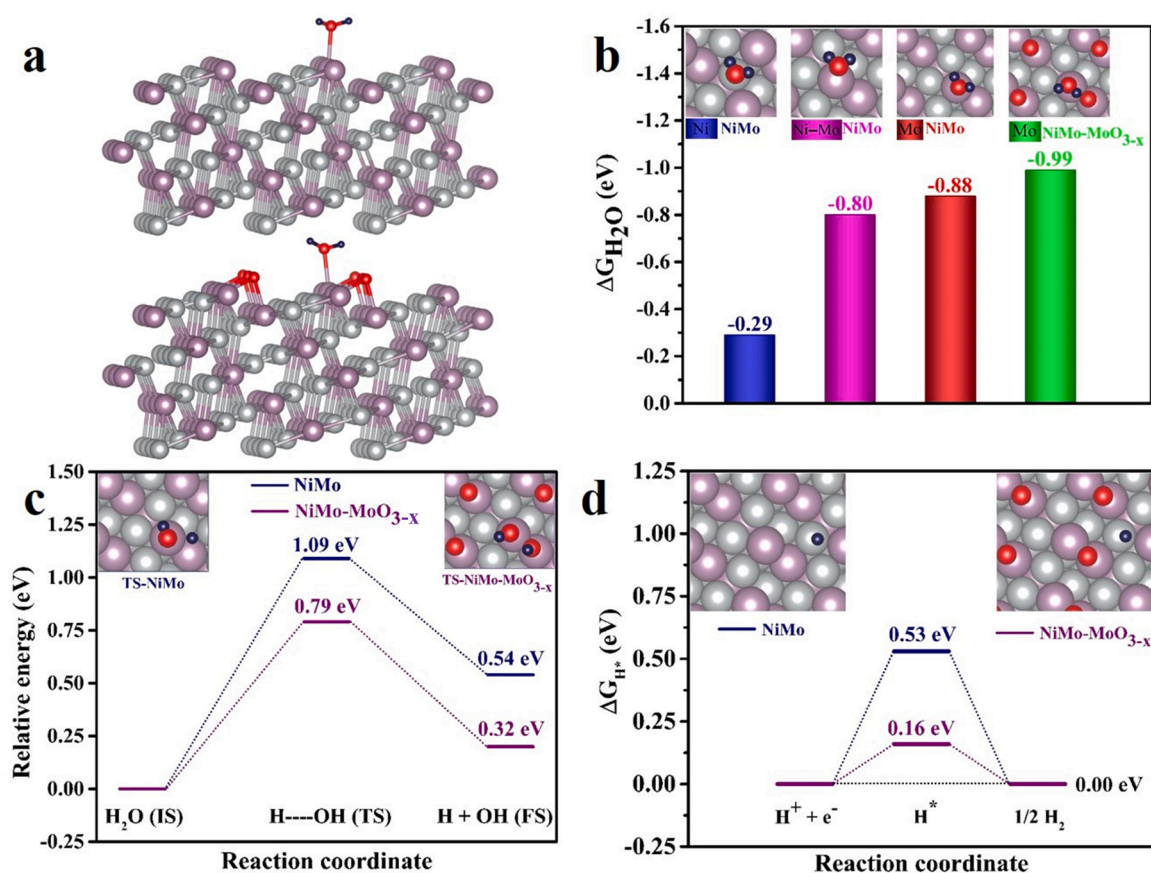
Fig. 8. a) Most stable optimized geometries of H_2O adsorbed NiMo and NiMo−MoO$_{3-x}$. b) Adsorption free energies of H_2O (ΔG_{H_2O}) on NiMo (blue at Ni center, magenta on Ni−Mo bond, and red at Mo center) and NiMo−MoO$_{3-x}$ (Mo center) surfaces. c) Potential energy of H_2O dissociation on NiMo and NiMo−MoO$_{3-x}$ surfaces. (d) Calculated hydrogen adsorption free energies (ΔG_{H^*}) on NiMo and NiMo−MoO$_{3-x}$ surfaces.

plots before and after CP testing (Fig. 9d) indicate that there was a slight improvement in the catalytic activity of NiMo-MoO$_{3-x}$ −PNR. These results further validate the excellent electrocatalytic stability and mechanical robustness of the NiMo-MoO$_{3-x}$ −PNR in an alkaline medium.

The structural stability of the catalyst after the cycle life test was confirmed using FESEM, HR-TEM and XPS analysis. FESEM images of NiMo-MoO$_{3-x}$ −PNR before and after 100,000 cycles (Fig. S14 a & b) proved its robust structural stability during cycling. In Fig. S14 c, the HR-TEM image of NiMo-MoO$_{3-x}$ −PNR showed lattice fringes with D-spacing of 0.20, 0.21, 0.22, and 0.24 nm, which were correspond to NiMo-alloy crystal planes (133), (331), (041), and (132), respectively. After cycle life, it can be observed that the NiMo-alloy crystal planes are maintained well. As shown in Fig. S15, the deconvoluted Ni-2p XPS peaks of NiMo-MoO$_{3-x}$ −PNR after cycle test exhibited mainly Ni-H$_{ad}$ (H-adsorbed in Ni) peaks along with Ni^0 and Ni^{2+} states, whereas, the deconvoluted Mo-3d consisted of Mo^{6+} state. Ni-H$_{ad}$ XPS peaks exhibited higher binding energy compared to the analogous Ni^0-peaks for the electron-deficient formation [63,64]. According to the theoretical study as shown in Fig. 8, Mo-center is more favorable for the adsorption of H_2O-molecule, promoting the dissociation of H−OH bond, and eventually attaching OH$^-$ to the Mo center, while H* adsorbed to the Ni center, resulting in H_2. For this repeated cycling processes, Ni-centers adsorbed sufficient H and the Mo surface converted to a higher oxidation state of 6 +, which was reflected in the XPS study. The presence of K (Fig. S15b) in the catalyst after cycle life indicates that KOH electrolyte penetrated inside the catalyst during the cycle. Interestingly, the BE of Ni^0-2p$_{3/2}$ (853.3 eV) and Mo^{6+}-3d$_{5/2}$ (231.33 eV) after 100,000 cycles was quite comparable to the BE of Ni^0-2p$_{3/2}$ (853.06 eV) and Mo^{6+}-3d$_{5/2}$ (231.34 eV) in NiMo-MoO$_{3-x}$ −PNR before cycling. These results imply that molybdenum oxides continue to experience the synergy effect with

alloy. As a result, the catalyst retains similar HER activity after 100,000 cycles. Overall, NiMo-MoO$_{3-x}$ −PNR demonstrated superior catalytic activity and excellent stability in HER in alkaline media, making it a promising and economical alternative to Pt/C in commercial scale electrocatalytic hydrogen production.

4. Conclusions

In summary, a novel porous NiMo-MoO$_{3-x}$ nanorod (NiMo-MoO$_{3-x}$ −PNR) as an efficient HER electrocatalyst in alkaline solution was successfully developed via generating a metal-organic framework, which exhibited a very low overpotential of only 24.5 mV at 10 mA cm^{-2} and a small Tafel slope of 32 mV dec^{-1}. Furthermore, its unaffected catalytic activity after 100,000 cycles and durability over 102 h indicate NiMo-MoO$_{3-x}$ −PNR possesses excellent stability, mass transport properties, and mechanical robustness in alkaline media. Its porous nanorod alloy-oxide hybrid structure was enabled by calcination of Ni-Mo-MOF−NR to NiMoO$_4$ −PNR and subsequent optimal thermal reduction of NiMoO$_4$ −PNR at 500 °C. In contrast, the direct reduction of Ni-Mo-MOF−NR produced nonporous NiMo-MoO$_{3-x}$/C−NPNR that exhibited much lower HER activity (overpotential: 51.0 mV at 10 mA cm^{-2}, Tafel slope: 56.4 mV dec^{-1}) than NiMo-MoO$_{3-x}$ −PNR. The superior performance of the electrocatalyst relative to powder NPGM-based electrocatalysts and parallel to state-of-the-art PGM-based electrocatalysts is attributed to its optimal porous nanorod structure, composition, and improved bifunctional properties of its alloy-oxide hybrid-structure as confirmed by theoretical studies. Thus, the present study has developed an innovative strategy for the design and synthesis of high-performance porous electrocatalyst for HER, and this invention may be helpful in designing various high-performance electrocatalysts.
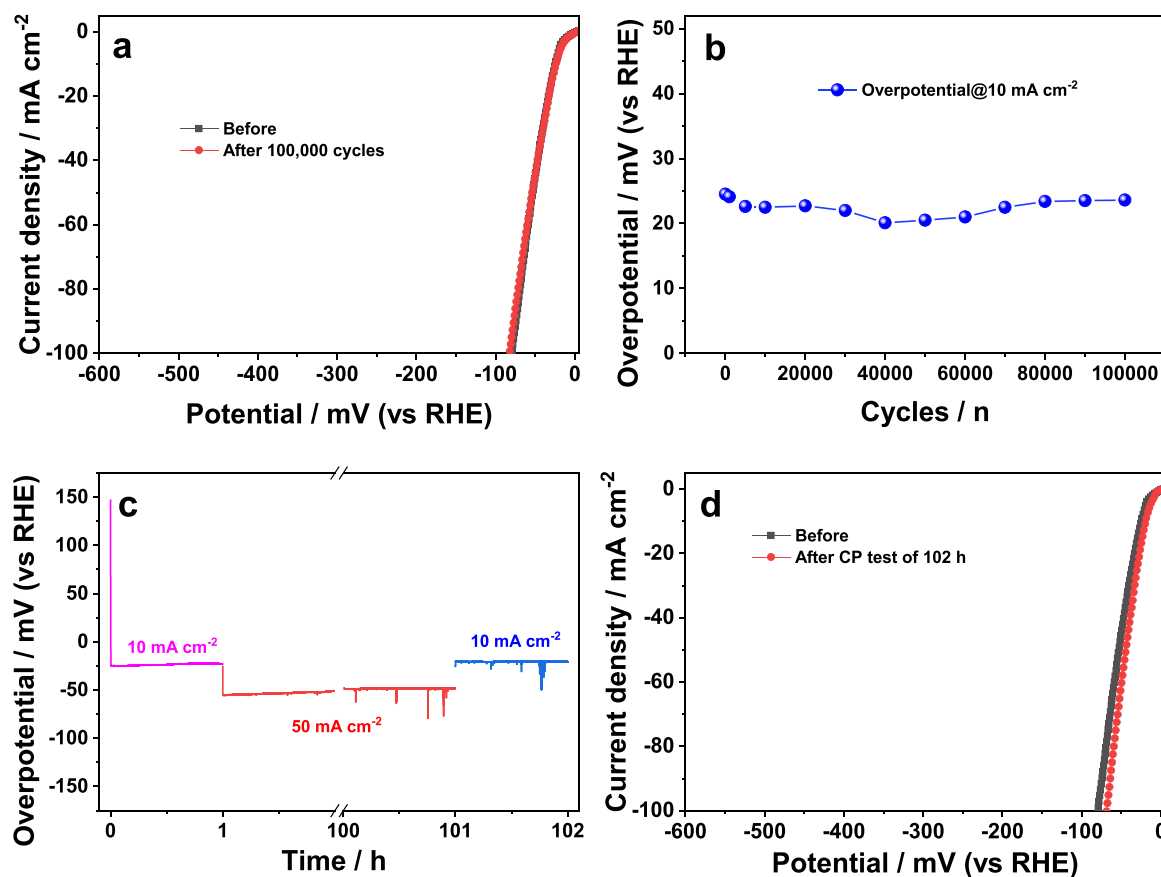
Fig. 9. Catalytic stability test of NiMo-MoO$_{3-x}$ −PNR: a) LSV plots before and after 100,000 CV cycles, b) overpotential during CV cycle test, c) durability test of NiMo-MoO$_{3-x}$ −PNR for 102 h by conducting successive CP tests at 10 mA cm^{-2} for 1 h, 50 mA cm^{-2} for 100 h, and 10 mA cm^{-2} for 1 h, d) LSV plots before after durability test.

CRediT authorship contribution statement

Bal Sydulu Singu: Conceptualization, Methodology, Data curation, Formal analysis, Writing – review & editing. **Debasish Mandal:** Writing – review & editing. **Ramesh Kumar Chitumalla:** Software, Writing – review & editing. **Yongrae Kim:** Data curation. **Gil Ho Kim:** Data curation. **Hoon Taek Chung:** Data curation. **Joonkyung Jang:** Software, Writing – review & editing. **Hansung Kim:** Funding acquisition, Investigation, Resources, Supervision, Writing – review & editing.

Declaration of Competing Interest

The authors declare that they have no known competing financial interests or personal relationships that could have appeared to influence the work reported in this paper.

Data availability

Data will be made available on request.

Acknowledgments

Appendix A. Supplementary material

Supplementary data associated with this article can be found in the online version at doi:10.1016/j.apcatb.2023.122421.

References

[1] P. Wang, X. Zhang, J. Zhang, S. Wan, S. Guo, G. Lu, J. Yao, X. Huang, Precise tuning in platinum-nickel/nickel sulfide interface nanowires for synergistic hydrogen evolution catalysis, Nat. Commun. 8 (2017) 1–9, https://doi.org/10.1038/ncomms14580.

[2] L. Zhang, Y. Jia, X. Yan, X. Yao, Activity origins in nanocarbons for the electrocatalytic hydrogen evolution reaction, Small 14 (2018) 1–15, https://doi.org/10.1002/smll.201800235.

[3] K. Liu, H. Zhong, F. Meng, X. Zhang, J. Yan, Q. Jiang, Recent advances in metal-nitrogen-carbon catalysts for electrochemical water splitting, Mater. Chem. Front. 1 (2017) 2155–2173, https://doi.org/10.1039/c7qm00119c.

[4] P. Li, R. Zhao, H. Chen, H. Wang, P. Wei, H. Huang, Q. Liu, T. Li, X. Shi, Y. Zhang, M. Liu, X. Sun, Recent advances in the development of water oxidation electrocatalysts at mild pH, Small 15 (2019) 1–27, https://doi.org/10.1002/smll.201805103.

[5] L. Han, S. Dong, E. Wang, Transition-metal (Co, Ni, and Fe)-based electrocatalysts for the water oxidation reaction, Adv. Mater. 28 (2016) 9266–9291, https://doi.org/10.1002/adma.201602270.

[6] J. Wang, W. Cui, Q. Liu, Z. Xing, A.M. Asiri, X. Sun, Recent progress in cobalt-based heterogeneous catalysts for electrochemical water splitting, Adv. Mater. 28 (2016) 215–230, https://doi.org/10.1002/adma.201502696.

[7] D. Huang, S. Li, Y. Luo, L. Liao, J. Ye, H. Chen, Selflated construction of 1D NiMo nanowires: via a Li electrochemical tuning method for the hydrogen evolution reaction, Nanoscale 11 (2019) 19429–19436, https://doi.org/10.1039/c9nr05311e.

[8] L. Yang, L. Zeng, H.H. Liu, Y. Deng, Z. Zhou, J. Yu, H.H. Liu, W. Zhou, Hierarchical microsphere of MoNi porous nanosheets as electrocatalyst and cocatalyst for hydrogen evolution reaction, Appl. Catal. B Environ. 249 (2019) 98–105, https://doi.org/10.1016/j.apcatb.2019.02.062.

[9] M. Fang, W. Gao, G. Dong, Z. Xia, S.P. Yip, Y. Qin, Y. Qu, J.C. Ho, Hierarchical NiMo-based 3D electrocatalysts for highly-efficient hydrogen evolution in alkaline conditions, Nano Energy 27 (2016) 247–254.

[10] S. Zhao, J. Huang, Y. Liu, J. Shen, H. Wang, X. Yang, Y. Zhu, C. Li, Multimetallic Ni-Mo/Cu nanowires as nonprecious and efficient full water splitting catalyst, J. Mater. Chem. A 5 (2017) 4207–4214, https://doi.org/10.1039/c6ta10749d.

[11] M.Y. Gao, C. Yang, Q.B. Zhang, J.R. Zeng, X.T. Li, Y.X. Hua, C.Y. Xu, P. Dong, Facile electrochemical preparation of self-supported porous Ni-Mo alloy microsphere films as efficient bifunctional electrocatalysts for water splitting, J. Mater. Chem. A 5 (2017) 5797–5805, https://doi.org/10.1039/c6ta10812a.

[12] J.-Y.Y. Zhang, T. He, M. Wang, R. Qi, Y. Yan, Z. Dong, H. Liu, H. Wang, B.Y. Xia, Energy-saving hydrogen production coupling urea oxidation over a bifunctional nickel-molybdenum nanotube array, Nano Energy 60 (2019) 894–902, doi.org/10.1016/j.nanoen.2019.04.035.

[13] Y. Zhou, M. Luo, W. Zhang, Z. Zhang, X. Meng, X. Shen, H. Liu, M. Zhou, X. Zeng, Topological Formation of a Mo-Ni-Based Hollow Structure as a Highly Efficient Electrocatalyst for the Hydrogen Evolution Reaction in Alkaline Solutions, ACS Appl. Mater. Interfaces 11 (2019) 21998–22004, doi/10.1021/acsami.9b03686.

[14] R.B. Patil, A. Mantri, S.D. House, J.C. Yang, J.R. McKone, Enhancing the performance of Ni-Mo alkaline hydrogen evolution electrocatalysts with carbon supports, ACS Appl. Energy Mater. 2 (2019) 2524–2533, https://doi.org/10.1021/acsaem.8b02087.

[15] Y.-Y. Chen, Y. Zhang, X. Zhang, T. Tang, H. Luo, S. Niu, Z.-H. Dai, L.-J. Wan, J.-S. Hu, Y. Chen, Z. Dai, Y. Zhang, X. Zhang, T. Tang, H. Luo, S. Niu, L. Wan, J. Hu, Self-templated fabrication of MoNi4/MoO3-x nanorod arrays with dual active components for highly efficient hydrogen evolution, Adv. Mater. 29 (2017), 1703311, https://doi.org/10.1002/ADMA.201703311.

[16] R. Tong, Z. Sun, X. Wang, S. Wang, H. Pan, Network-like Ni1−xMox nanosheets: multi-functional electrodes for overall water splitting and supercapacitor, ChemElectroChem 6 (2019) 1338–1343, https://doi.org/10.1002/celc.201801725.

[17] J.R. McKone, B.F. Sadtler, C.A. Werlang, N.S. Lewis, H.B. Gray, Ni-Mo nanopowders for efficient electrochemical hydrogen evolution, ACS Catal. 3 (2013) 166–169, https://doi.org/10.1021/cs300691m.

[18] W. Gao, W. Gou, X. Zhou, J.C. Ho, Y. Ma, Y. Qu, Amine-Modulated/Engineered Interfaces of NiMo Electrocatalysts for Improved Hydrogen Evolution Reaction in Alkaline Solutions, 10 (2017) 1728-1733, doi.org/10.1021/acsami.7b16125.

[19] J. Zhang, T. Wang, P. Liu, Z. Liao, S. Liu, X. Zhuang, M. Chen, E. Zschech, X. Feng, Efficient hydrogen production on MoNi4 electrocatalysts with fast water dissociation kinetics, Nat. Commun. 8 (2017) 1–8, https://doi.org/10.1038/ncomms15437.

[20] C. Li, J.B. Baek, The promise of hydrogen production from alkaline anion exchange membrane electrolyzers, Nano Energy 87 (2021), 106162, https://doi.org/10.1016/j.nanoen.2021.106162.

[21] N. Du, C. Roy, R. Peach, M. Turnbull, S. Thiele, C. Bock, Anion-exchange membrane water electrolyzers, Chem. Rev. 122 (2022) 11830–11895, https://doi.org/10.1021/acs.chemrev.1c00854.

[22] H.J.W. Li, K. Liu, J. Fu, K. Chen, K. Yang, Y. Lin, B. Yang, Q. Wang, H. Pan, Z. Cai, H. Li, M. Cao, J. Hu, Y.R. Lu, T.S. Chan, E. Cortés, A. Fratalocchi, M. Liu, Paired Ru–O–Mo ensemble for efficient and stable alkaline hydrogen evolution reaction, Nano Energy 82 (2021), 105767, https://doi.org/10.1016/J.NANOEN.2021.105767.

[23] X. Lu, M. Cai, Z. Zou, J. Huang, C. Xu, A novel MoNi@Ni(OH)2 heterostructure with Pt-like and stable electrocatalytic activity for the hydrogen evolution reaction, Chem. Commun. 56 (2020) 1729–1732, https://doi.org/10.1039/c9cc08985c.

[24] N. Danilovic, R. Subbaraman, D. Strmcnik, K.-C. Chang, A.P. Paulikas, V. R. Stamenkovic, N.M. Markovic, Enhancing the alkaline hydrogen evolution reaction activity through the bifunctionality of Ni(OH)2/metal catalysts, Angew. Chem. 124 (2012) 12663–12666, https://doi.org/10.1002/ange.201204842.

[25] J. Li, B. Li, H. Huang, S. Yan, C. Yuan, N. Wu, D. Guo, X. Liu, Polyvinylpyrrolidone gel based Pt/Ni(OH)2 heterostructures with redistributing charges for enhanced alkaline hydrogen evolution reaction, J. Mater. Chem. A 9 (2021) 27061–27071, https://doi.org/10.1039/D1TA06149F.

[26] L. Yang, H. Liu, Z. Zhou, Y. Chen, G. Xiong, L. Zeng, Y. Deng, X. Zhang, H. Liu, W. Zhou, A. universal process: self-templated and oriented fabrication of XMoO4 (X: Ni, Co, or Fe) nanosheets on MoO2 nanoplates as electrocatalysts for efficient water splitting, cite this, ACS Appl. Mater. Interfaces 12 (2020) 33785–33794, https://doi.org/10.1021/acsami.0c08750.

[27] X. Liu, L. Zhang, J. Wang, Design strategies for MOF-derived porous functional materials: preserving surfaces and nurturing pores, J. Mater. 7 (2021) 440–459, https://doi.org/10.1016/j.jmat.2020.10.008.

[28] G. Kresse, J. Hafner, Ab initio molecular dynamics for liquid metals, Phys. Rev. B 47 (1993) 558–561, https://doi.org/10.1103/PhysRevB.47.558.

[29] N.N.T. Pham, S.G. Kang, H.J. Kim, C. Pak, B. Han, S.G. Lee, Catalytic activity of Ni3Mo surfaces for hydrogen evolution reaction: a density functional theory approach, Appl. Surf. Sci. 537 (2021) 147894, https://doi.org/10.1016/j.apsusc.2021.147894.

[30] P.E. Blöchl, Projector augmented-wave method, Phys. Rev. B 50 (1994) 17953–17979, https://doi.org/10.1103/PhysRevB.50.17953.

[31] J.P. Perdew, K. Burke, M. Ernzerhof, Generalized gradient approximation made simple, Phys. Rev. Lett. 77 (1996) 3865–3868, https://doi.org/10.1103/PhysRevLett.77.3865.

[32] R.K. Chitumalla, K. Kim, X. Gao, J. Jang, A density functional theory study on the underwater adhesion of catechol onto a graphite surface, Phys. Chem. Chem. Phys. 23 (2021) 1031–1037, https://doi.org/10.1039/d0cp05623e.

[33] D. Li, Z. Li, R. Zou, G. Shi, Y. Huang, W. Yang, W. Yang, C. Liu, X. Peng, Coupling overall water splitting and biomass oxidation via Fe-doped Ni2P@C nanosheets at large current density, Appl. Catal. B Environ. 307 (2022) 121170, https://doi.org/10.1016/j.apcatb.2022.121170.

[34] Z. Zhang, J. Ren, J. Xu, Z. Wang, W. He, S. Wang, X. Yang, X. Du, L. Meng, P. Zhao, Adjust the arrangement on the metal-organic framework to obtain hybrid proton exchange membrane with long-term stable high proton conductivity, J. Membr. Sci. 607 (2020), 118194, https://doi.org/10.1016/J.MEMSCI.2020.118194.

[35] A.B. Lysenko, G.A. Senchyk, J. Lincke, D. Lässig, A.A. Fokin, E.D. Butova, P. R. Schreiner, H. Krautscheid, K.V. Domasevitch, Metal oxide-organic frameworks (MOOFs), a new series of coordination hybrids constructed from molybdenum(vi) oxide and bitopic 1,2,4-triazole linkers, Dalton Trans. 39 (2010) 4223–4231, https://doi.org/10.1039/B922732F.

[36] J. Yuan, D. Yao, L. Jiang, Y. Tao, J. Che, G. He, H. Chen, Mn-doped NiMoO4 mesoporous nanorods/reduced graphene oxide composite for high-performance all-solid-state supercapacitor, ACS Appl. Energy Mater. 3 (2020) 1794–1803, https://doi.org/10.1021/acsaem.9b02238.

[37] G. Kianpour, M. Salavati-Niasari, H. Emadi, Sonochemical synthesis and characterization of NiMoO4 nanorods, Ultrason. Sonochem. 20 (2013) 418–424, https://doi.org/10.1016/j.ultsonch.2012.08.012.

[38] D. Mandal, P. Routh, A.K. Nandi, Quantum-dot-mediated controlled synthesis of dual oxides of molybdenum from MoS2: quantification of supercapacitor efficacy, Chem. Asian J. 13 (2018) 3871–3884, https://doi.org/10.1002/asia.201801173.

[39] N. Maheswari, G. Muralidharan, Controlled synthesis of nanostructured molybdenum oxide electrodes for high performance supercapacitor devices, Appl. Surf. Sci. 416 (2017) 461–469, https://doi.org/10.1016/j.apsusc.2017.04.094.

[40] A. Wu, C. Tian, H. Yan, Y. Jiao, Q. Yan, G. Yang, H. Fu, Hierarchical MoS2@MoP core-shell heterojunction electrocatalysts for efficient hydrogen evolution reaction over a broad pH range, Nanoscale 8 (2016) 11052–11059, https://doi.org/10.1039/c6nr02803a.

[41] J. Yang, Y. Ouyang, H. Zhang, H. Xu, Y. Zhang, Y. Wang, Novel Fe2P/graphitized carbon yolk/shell octahedra for high-efficiency hydrogen production and lithium storage, J. Mater. Chem. A 4 (2016) 9923–9930, https://doi.org/10.1039/c6ta03501a.

[42] A. Cetin, E.N. Esenturk, Hierarchical nanowire and nanoplate-assembled NiCo2O4–NiO biphasic microspheres as effective electrocatalysts for oxygen evolution reaction, Mater. Today Chem. 14 (2019), 100215, https://doi.org/10.1016/j.mtchem.2019.100215.

[43] H. Jiang, L. Yan, S. Zhang, Y. Zhao, X. Yang, Y. Wang, J. Shen, X. Zhao, L. Wang, Electrochemical surface restructuring of phosphorus-doped carbon@MoP electrocatalysts for hydrogen evolution, Nano-Micro Lett. 13 (2021) 1–15, https://doi.org/10.1007/S40820-021-00737-W/FIGURES/6.

[44] M.G. Radhika, B. Gopalakrishna, K. Chaitra, L.K.G. Bhatta, K. Venkatesh, M. K. Sudha Kamath, N. Kathyayini, Electrochemical studies on Ni, Co & Ni/Co-MOFs for high-performance hybrid supercapacitors, Mater. Res. Express 7 (2020), 054003, https://doi.org/10.1088/2053-1591/AB8D5D.

[45] D.D. Rodene, E. Eladgham, R.B. Gupta, I.U. Arachchige, V. Tallapally, Crystal structure and composition-dependent electrocatalytic activity of Ni–Mo nanoalloys for water splitting to produce hydrogen, ACS Appl. Energy Mater. 2 (2019) 7112–7120, https://doi.org/10.1021/acsaem.9b01043.

[46] D. Mandal, P. Routh, A.K. Nandi, A new facile synthesis of tungsten oxide from tungsten disulfide: structure dependent supercapacitor and negative differential resistance properties, Small 14 (2018) 1–13, https://doi.org/10.1002/smll.201702881.

[47] D. Mandal, A.Y. Jeong, B.S. Singu, S. Lee, W.J. Mun, H. Kim, Flexible all solid-state niobium nitride//activated carbon lithium-ion hybrid capacitor with high volumetric power and energy densities, J. Energy Storage 48 (2022), 104031, https://doi.org/10.1016/j.est.2022.104031.

[48] R. Nyholm, N. Martensson, Core level binding energies for the elements Zr-Te (Z=40-52), J. Phys. C Solid State Phys. 13 (1980) L279–84, https://doi.org/10.1088/0022-3719/13/11/008.

[49] L. Lin, M. Chen, L. Wu, Synthesis of molybdenum–tungsten bimetallic carbide hollow spheres as pH-universal electrocatalysts for efficient hydrogen evolution reaction, Adv. Mater. Interfaces 5 (2018) 1–9, https://doi.org/10.1002/admi.201801302.

[50] X. Jiang, H. Jang, S. Liu, Z. Li, M.G. Kim, C. Li, Q. Qin, X. Liu, J. Cho, The heterostructure of Ru2P/WO3/NPC synergistically promotes H2O dissociation for improved hydrogen evolution, Angew. Chem. Int. Ed. 60 (2021) 4110–4116, https://doi.org/10.1002/anie.202014411.

[51] X. Yang, A.Y. Lu, Y. Zhu, M.N. Hedhili, S. Min, K.W. Huang, Y. Han, L.J. Li, CoP nanosheet assembly grown on carbon cloth: a highly efficient electrocatalyst for hydrogen generation, Nano Energy 15 (2015) 634–641, https://doi.org/10.1016/j.nanoen.2015.05.026.

[52] S. Fletcher, Tafel slopes from first principles, J. Solid State Electrochem. 13 (2009) 537–549, https://doi.org/10.1007/s10008-008-0670-8.

[53] Z. Zhuang, J. Huang, Y. Li, L. Zhou, L. Mai, The holy grail in platinum-free electrocatalytic hydrogen evolution: molybdenum-based catalysts and recent advances, ChemElectroChem 6 (2019) 3570–3589, https://doi.org/10.1002/celc.201900143.

[54] J. Chen, G. Qian, H. Zhang, S. Feng, Y. Mo, L. Luo, S. Yin, J. Chen, G. Qian, H. Zhang, S. Feng, Y. Mo, L. Luo, S. Yin, PtCo@PtSn heterojunction with high stability/activity for pH-universal H2 evolution, Adv. Funct. Mater. 32 (2022), 2107597, https://doi.org/10.1002/ADFM.202107597.

[55] W. Li, H. Zhang, K. Zhang, W. Hu, Z. Cheng, H. Chen, X. Feng, T. Peng, Z. Kou, Monodispersed ruthenium nanoparticles interfacially bonded with defective

nitrogen-and-phosphorus-doped carbon nanosheets enable pH-universal hydrogen evolution reaction, Appl. Catal. B Environ. 306 (2022) 121095, https://doi.org/10.1016/J.APCATB.2022.121095.

[56] A. Mosallanezhad, C. Wei, P. Ahmadian Koudakan, Y. Fang, S. Niu, Z. Bian, B. Liu, T. Huang, H. Pan, G. Wang, Interfacial synergies between single-atomic Pt and CoS for enhancing hydrogen evolution reaction catalysis, Appl. Catal. B Environ. 315 (2022), 121534, https://doi.org/10.1016/J.APCATB.2022.121534.

[57] C. Li, H. Jang, M.G. Kim, L. Hou, X. Liu, J. Cho, Ru-incorporated oxygen-vacancy-enriched MoO2 electrocatalysts for hydrogen evolution reaction, Appl. Catal. B Environ. 307 (2022) 121204, https://doi.org/10.1016/J.APCATB.2022.121204.

[58] K. Xu, H. Cheng, H. Lv, J. Wang, L. Liu, S. Liu, X. Wu, W. Chu, C. Wu, Y. Xie, Controllable surface reorganization engineering on cobalt phosphide nanowire arrays for efficient alkaline hydrogen evolution reaction, Adv. Mater. 30 (2018), https://doi.org/10.1002/adma.201703322.

[59] X. Liu, K. Ni, C. Niu, R. Guo, W. Xi, Z. Wang, J. Meng, J. Li, Y. Zhu, P. Wu, Q. Li, J. Luo, X. Wu, L. Mai, Upraising the O 2p orbital by integrating Ni with MoO 2 for accelerating hydrogen evolution kinetics, ACS Catal. 9 (2019) 2275–2285, https://doi.org/10.1021/acscatal.8b04817.

[60] H. Wu, W. Xiao, C. Guan, X. Liu, W. Zang, H. Zhang, J. Ding, Y.P. Feng, S. J. Pennycook, J. Wang, Hollow Mo-doped CoP nanoarrays for efficient overall water splitting, Nano Energy 48 (2018) 73–80, https://doi.org/10.1016/j.nanoen.2018.03.034.

[61] J. Xiao, Z. Zhang, Y. Zhang, Q. Lv, F. Jing, K. Chi, S. Wang, Large-scale printing synthesis of transition metal phosphides encapsulated in N, P co-doped carbon as highly efficient hydrogen evolution cathodes, Nano Energy 51 (2018) 223–230, https://doi.org/10.1016/j.nanoen.2018.06.040.

[62] J. Tian, N. Cheng, Q. Liu, X. Sun, Y. He, A.M. Asiri, Self-supported NiMo hollow nanorod array: an efficient 3D bifunctional catalytic electrode for overall water splitting, J. Mater. Chem. A 3 (2015) 20056–20059, https://doi.org/10.1039/c5ta04723d.

[63] J. Tang, S. Yamamoto, T. Koitaya, Y. Yoshikura, K. Mukai, S. Yoshimoto, I. Matsuda, J. Yoshinobu, Hydrogen adsorption and absorption on a Pd-Ag alloy surface studied using in-situ X-ray photoelectron spectroscopy under ultrahigh vacuum and ambient pressure, Appl. Surf. Sci. 463 (2019) 1161–1167, https://doi.org/10.1016/j.apsusc.2018.07.078.

[64] S.J. Kerber, J.J. Bruckner, K. Wozniak, S. Seal, S. Hardcastle, T.L. Barr, The nature of hydrogen in x-ray photoelectron spectroscopy: general patterns from hydroxides to hydrogen bonding, J. Vac. Sci. Technol. A Vac. Surf. Films 14 (1996) 1314–1320, https://doi.org/10.1116/1.579947.